Applied Catalysis B: Environmental 146 (2014) 105–111

Contents lists available at ScienceDirect

Applied Catalysis B: Environmental

journal homepage: www.elsevier.com/locate/apcatb

Mg and Al substituted cobalt spinels as catalysts for low temperature deN_2O—Evidence for octahedral cobalt active sites

P. Stelmachowski*, G. Maniak, J. Kaczmarczyk, F. Zasada, W. Piskorz, A. Kotarba, Z. Sojka

Jagiellonian University, ul. Ingardena 3, Krakow 30-060, Poland

ARTICLE INFO

Article history:
Received 30 October 2012
Received in revised form 2 May 2013
Accepted 13 May 2013
Available online 18 May 2013

Keywords:
Cobalt spinel
N_2O decomposition
Nitrous oxide
Catalyst
Active sites

ABSTRACT

A series of cobalt spinel oxides with the chemical composition: Co_3O_4, $MgCo_2O_4$, $MgCoAlO_4$, $CoAl_2O_4$, $Mg_{0.5}Co_{0.5}Al_2O_4$ and $MgAl_2O_4$ was synthesised, characterised and studied for catalytic decomposition of N_2O. Selective replacement of cobalt ions in the tetrahedral and octahedral sites was employed to probe the specific activity of both types of centres. The combined experimental XRD, UV–vis, RS, XPS, BET, TPR, Temperature Programmed Catalytic Reaction (TPCatR) methods and DFT modelling allowed to explore the mechanistic role of the coordination (tetrahedral, octahedral) and valence (+2, +3) states of cobalt ions in the Co_3O_4 spinel matrix. The prime active sites of deN_2O reaction were definitely identified as the octahedral Co^{3+} ions (E_a = 15–17 kcal mol^{-1}), whereas the tetrahedral Co^{2+} ions were found to be clearly much less active (E_a = 27–28 kcal mol^{-1}).

© 2013 Elsevier B.V. All rights reserved.

1. Introduction

The catalytic deN_2O reaction is of great environmental relevance since nitrous oxide has been recognized as one of the most important greenhouse gases with lifetime of 150 years in the atmosphere and global warming potential of 310 [1]. The high temperature of simple thermal decomposition of N_2O, over 600 °C, causes the catalytic decomposition as the only economic solution for practical applications.

Among a large variety of the investigated deN_2O catalysts such as supported noble metals [2,3], pure [4] and mixed metal oxides [5–7] or metallozeolites [8], the most promising are the catalysts based on cobalt spinel, which show high conversion already below 400 °C [9–11]. Furthermore, their activity can be effectively promoted by bulk and surface doping [11,12]. In the case of the metallozeolite catalytic systems with low transition metal ions content, the active sites are thought to be the cations the in divalent state: Fe^{2+}, Cu^{2+} or Co^{2+} [13]. Yet, it should be noted that the postulated reaction mechanism is different that that operating for oxide catalysts, since the surface diffusion of intermediates is not considered to be an important reaction step.

A large group of mixed valence metal oxides crystallizes in spinel structure with metal ions located in tetrahedral and octahedral sites. These compounds are represented by a general formula AB_2O_4, where, in the most cases, A and B are divalent and trivalent cations (2–3 spinels), respectively [14]. Spinels which contain transition metal oxides are widely investigated as active catalysts for low temperature decomposition of nitrous oxide, operating along the cationic redox mechanism [15]. It is triggered by electron transfer from catalyst surface to N_2O, leading to its immediate dissociation into N_2 and O^- [16], followed by diffusion of surface O^- intermediates and recombination of surface oxygen into O_2 molecule, closing the catalytic cycle. Since all these steps exhibit a redox character, there is a strong correlation between the electronic properties (gauged, e.g., by catalyst work function) and the catalyst activity, documented elsewhere [11,17,18].

Addition of CeO_2 to cobalt spinel has shown to lead to enhanced catalytic activity in the direct decomposition of N_2O. This effect has been ascribed to easier reduction of Co^{3+} to Co^{2+} by facilitating the desorption of adsorbed oxygen species, [19], however, this conjecture has not been definitely resolved. Analysis of deN_2O performance of various spinel AB_2O_4 catalysts, (where A = Mg, Ca, Mn, Co, Ni, Cu, Cr, Fe, Zn and B = Cr, Fe, Co) suggest that the catalysts that preserved octahedral cobalt ions ($MgCo_2O_4$, $ZnCo_2O_4$ and Co_3O_4) exhibit highest catalytic activity [20]. The observed loss of the catalyst activity was attributed to the surface reduction of Co(III) to Co(II) and segregation of cobalt(II) in the form a CoO phase [21]. However, despite a large number of papers dealing with decomposition of N_2O, the nature of the actual active sites for the bulk cobalt spinel catalyst: octahedral or tetrahedral, cobalt(II) or (III) ions has

* Corresponding author. Tel.: +48 6632246; fax: +48 12 6340515.
E-mail address: pawel.stelmachowski@uj.edu.pl (P. Stelmachowski).

0926-3373/$ – see front matter © 2013 Elsevier B.V. All rights reserved.
http://dx.doi.org/10.1016/j.apcatb.2013.05.027

not been systematically examined. The aim of this work was to explore the mechanistic role of the coordination (tetrahedral, octahedral) and valence (+2, +3) states of cobalt ions in the Co_3O_4 spinel catalyst by selective substitution of the redox Co^{2+} (Co^T) and Co^{3+} (Co^O) active sites by non-redox Mg^{2+} and Al^{3+} ions, respectively. This goal was accomplished by synthesis of series of spinel catalyst intentionally modulated composition (Co_3O_4, $MgCo_2O_4$, Co_2AlO_4, $CoAl_2O_4$, $MgAl_2O_4$), their thorough characterization and catalytic deN_2O test studies.

2. Materials and methods

The mixed oxide spinels $A_{3-x}B_xO_4$ (A, B = Mg, Al, Co) were obtained by precipitation with ammonium carbonate of the corresponding nitrate precursors and (Aldrich). Precipitation was carried out until pH ~9 was reached and then the resultant solid was rinsed to pH = 7. In the case of $MgAl_2O_4$ the precursor was precipitated from the solution containing polyvinyl alcohol (Aldrich). In order to obtain spinel structure of the final oxide the precipitates were dried at 100 °C and calcined at 600–900 °C. Selected temperatures of calcination are higher than the temperatures required for decomposition of the precursors, especially for Co_3O_4 and $MgCo_2O_4$, but were chosen so as to exceed the temperatures attained in the catalytic tests. The elemental Co, Mg and Al composition was confirmed by XRF method (Thermoscientific, ARL QUANT'X). The TPR experiments were performed on a Quantachrome ChemBET Pulsar TPR-TPD instrument with TCD detector using 5% H_2/Ar and heating rate of 10 °C min^{-1}.

The phase composition of the catalyst samples was examined by X-ray diffraction, using CuKα radiation by means of a X'pert Pro Philips diffractometer. Data were recorded in the 2θ range of 10–80° with the resolution of 0.02°. The analysis of diffractograms was performed on the basis of the Williamson–Hall equation to obtain the crystallite sizes, and the Rietveld method was applied to determine the unit cell parameters (DBWS9807a programme) [22]. Diffuse reflectance UV–vis spectra (DRS) were collected with a Perkin Elmer Lambda 12 spectrometer. $BaSO_4$ was the reference as well as a medium for the dilution of the samples and the spectra were recorded in the range of 200–900 nm in ambient conditions. The micro-Raman spectra were recorded at room temperature using a Renishaw InVia spectrometer equipped with a Leica DMLM confocal microscope and a CCD detector with an excitation wavelength of 785 nm. The laser power for 20× magnification lens was 1.5 mW except for the $Mg_{0.5}Co_{0.5}Al_2O_4$ and $MgAl_2O_4$, where it was set to ~15 mW and maximum power of 300 mW, respectively. The Raman scattered light was collected in the spectral range of 150–850 cm^{-1}. The X-ray photoelectron spectra (XPS) were measured with a Prevac photoelectron spectrometer equipped with a hemispherical VG SCIENTA R3000 analyzer. The spectra were recorded using a monochromatized aluminium AlKα source (E = 1486.6 eV) and an electron flood gun (FS40A-PS) to compensate the residual charge on the surface. The background pressure in the chamber during the measurements was 5×10^{-9} mbar. Before spectra acquisition the samples were outgassed at c.a. 50 °C for at least 15 min. The spectra were recorded with a pass energy of 100 eV for the survey and narrow scans. All the binding energies were referenced to the C 1s peak at 285 eV of the adventitious carbon. The Tougaard, Shirley and linear type baselines implemented in CasaXPS software were applied prior the analysis of the area of the photopeaks and estimation of the integration error.

The Temperature Programmed Catalytic Reaction (TPCatR) measurements of N_2O decomposition in the range of 20–900 °C were performed in a quartz flow reactor with quasi-ideal mixing using 300 mg of the catalyst (sieve fraction of 0.2–0.3 mm, bed height ~1 mm). The flow rate of the feed of 30 ml min^{-1} (5% N_2O in He, 7000 h^{-1}) and the heating rate of 10 °C min^{-1} were used. The progress of the reaction was monitored by a quadruple mass spectrometer (SRS RGA200, m/z = 44, 32, 30, 28 and 18). The experimental data of TPCatR measurements expressed as N_2O conversion (X_{N_2O}) versus temperature (T) were fitted with the kinetic model for the flow reactor with quasi ideal mixing: $k\tau = X_{N_2O}/(1 - X_{N_2O})$ [23]. The kinetic parameters such the rate constants (k) at 400 °C of N_2O decomposition and the apparent activation energies (E_a/kJ mol^{-1}), were then determined using the Arrhenius formula $k = A \cdot e^{-(E_a/RT)}$. To ensure that the reactor is operating in the kinetic regime and to satisfy and to satisfy the considered reactor model [24] the criterial numbers for extra- and intra-granular diffusion limitations were checked according to the Eurokin procedure [25]. The first order kinetics was assumed on the basis of analysis of molecular level mechanism of the N_2O decomposition [4], supported by available experimental data [26,27]. The turnover rates (TOR/s^{-1}) were calculated from the reaction rate (r/$nmol_{N_2O} \times m^{-2} \times s^{-1}$) with the use of the XPS-derived surface composition and the number of the exposed cations on the dominant (1 0 0) crystallographic plane [28] using the elementary cell length obtained from form XRD.

For all calculations (VASP Package [29]) the DFT + U scheme [30] (with U parameter of 4.5 and 6.5 eV for Co^{3+} and Co^{2+}, respectively) with the projector augmented plane wave (PAW) [31] and PBE gradient corrected exchange-functional and the cutoff energy of 400 eV were used. Geometry optimization was performed until the net forces acting upon the ions were smaller than 1×10^{-2} eV $Å^{-1}$. Surface geometry was constructed by cleaving the spinel in the normal $\langle 1\,0\,0 \rangle$ direction with a vacuum separation of 15 Å between two periodically repeated slabs. In the adopted computational model both the stoichiometry of the bulk and the 1:2 ratio between the octahedral and tetrahedral ions were preserved.

3. Results and discussion

3.1. XRD and UV–vis bulk characterization

Representative XRD patterns of the investigated spinel catalysts obtained by replacement of cobalt in the tetrahedral and octahedral sites by magnesium and/or aluminium ions, respectively, are shown in Fig. 1a–f. The X-ray diffraction lines characteristic of the cobalt spinel structure were indexed within the Fd3m space group (24210-ICSD for Co_3O_4 and 24492-ICSD for $MgAl_2O_4$). The diffractograms proved spinel structure of the investigated samples, revealing no major structural changes upon modifications of the parent oxide and absence of any spurious phases. The size of crystallites and the unit cell parameters for all samples are summarized in Table 1.

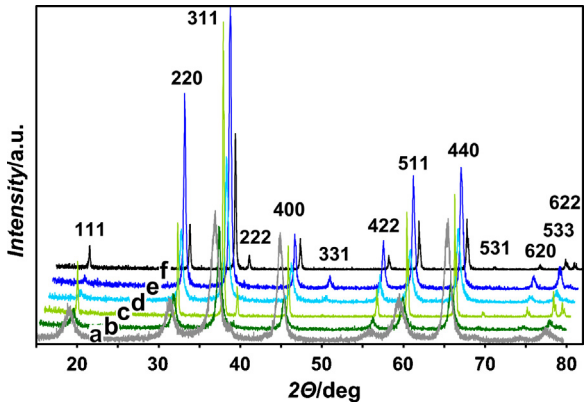

Fig. 1. XRD patterns of (a) $MgAl_2O_4$; (b) $MgCoAlO_4$; (c) $MgCo_2O_4$; (d) $Mg_{0.5}Co_{0.5}Al_2O_4$; (e) $CoAl_2O_4$ and (f) Co_3O_4, catalysts.

Table 1
Comparison of experimental ([a]) and calculated ([b]) structural parameters for the investigated spinel catalysts.

	$MgAl_2O_4$	$MgCoAlO_4$	$MgCo_2O_4$	$Mg_{0.5}Co_{0.5}Al_2O_4$	$CoAl_2O_4$	Co_3O_4
$S_{BET}/m^2\,g^{-1}$	67	61	6.1	69	34	10.4
D_{XRD}/nm	10	11	267	19	21	206
$a/Å$	8.076	8.080	8.081[a] 8.151[b]	8.081	8.090[a] 8.170[b]	8.085[a] 8.161[b]
u	0.258	0.260	0.264[a] 0.264[b]	0.262	0.259[a] 0.260[b]	0.264[a] 0.263[b]

For Co_3O_4, neglecting possible small inversion, the half-filled octahedral sites contain the diamagnetic $Co^{3+}(d^6, S=0)$ cations, whereas the tetrahedral sites, exhibiting one-eight occupancy are filed by the paramagnetic $Co^{2+}(d^7, S=3/2)$ cations. The distance between the nearest octahedral cobalt cations is equal to 2.89 Å, whereas for tetrahedral cobalt species the separation increases to 8.051 Å. This results from the edge connection between the structural octahedra and spatial separation of the tetrahedra connected by the corners only. In the first case the orbitals of neighbouring Co^{3+} partially overlap, allowing for easier migration of electrons within the octahedral stripes (vide infra). The detailed description of the Co_3O_4 structure and its nano-morphology was published by us elsewhere [28]. Introduction of magnesium into the spinel did not change the lattice parameters significantly nor the ions position within the Co_3O_4 oxide framework (Table 1). However, for the cobalt aluminate spinel an increase of the lattice constant (a) and decrease of the u parameter (defining the position of oxygen anions in the spinel lattice) led to the resultant slight modifications of the Co—O bond lengths in both the tetrahedral and the octahedral units by −0.06 and +0.03 Å, respectively.

The optical diffuse reflectance spectra for the investigated samples are shown in Fig. 2. Whereas $MgAl_2O_4$ is transparent in UV–vis (Fig. 2f) for Co_3O_4 and $MgCo_2O_4$ (Fig. 2a and b) the observed spectra are typical for the cobalt spinel [32]. The broad band at 1.6–1.9 eV is assigned to overlapping signals due to $t_{2g}(Co^{3+}) \rightarrow t_2(Co^{2+})$ MMCT (1.65 eV) transition and $^1A_1 \rightarrow {}^1T_1$ d–d transition of the low spin octahedral Co^{3+} ions. The latter feature is more clearly seen in Fig. 5c due to the absence of the MMCT band in the $MgCoAlO_4$ spinel. A very broad absorption in the range 2.3–2.9 eV (Fig. 5a and b) can arise from $p(O^{2-}) \rightarrow t_2(Co^{2+})$ LMCT transition at about 2.4 eV and $p(O^{2-}) \rightarrow e_g(Co^{3+})$ LMCT transition at about 2.8 eV [33]. In the case of the $CoAl_2O_4$ and $Mg_{0.5}Co_{0.5}Al_2O_4$ spinels containing only the tetrahedral cobalt (Fig. 5d and e), the UV–vis spectrum is dominated by a characteristic triplet at 1.96, 2.11 and 2.26 eV due to the spin-forbidden $^4A_2(F) \rightarrow {}^2T_1(G)$, $^2E(G)$, spin-allowed $^4A_2(F) \rightarrow {}^4T_1(P)$, and spin-forbidden $^4A_2(F) \rightarrow {}^2T_2(G)$ transitions in the tetracoordinated Co^{2+} [34]. The spin-forbidden bands appear at relatively high intensity because the involved doublet states are very close in energy to $^4T_1(P)$, which allows for their mixing. In an alternative interpretation proposed elsewhere [35], this triplet is associated with the splitting of the $^4A_2(F) \rightarrow {}^4T_1(P)$ band due to the Jahn–Teller distortion of the tetrahedral Co^{2+} ions. However, regardless the actual origin of this splitting, the UV–vis data confirm that the intended selective substitutions of the tetrahedral Co^{2+} and octahedral Co^{3+} cations by Mg^{2+} and Al^{3+} ions, respectively, have been successfully accomplished.

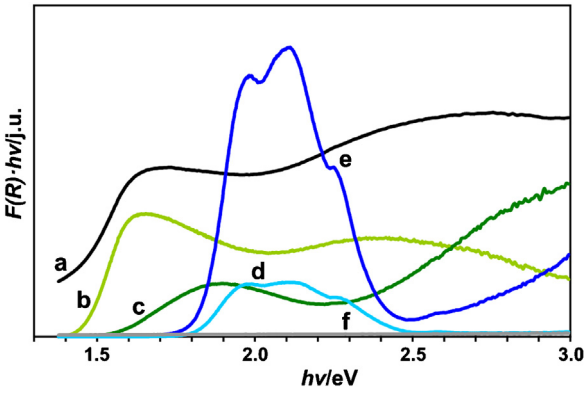

Fig. 2. The normalized Kubelka–Munk optical diffuse reflectance spectra (DRS) converted to absorption for samples: (a) Co_3O_4; (b) $MgCo_2O_4$; (c) $MgCoAlO_4$; (d) $Mg_{0.5}Co_{0.5}Al_2O_4$; (e) $CoAl_2O_4$ and (f) $MgAl_2O_4$.

3.2. Raman spectroscopy

The Raman spectra of Co_3O_4, presented in Fig. 3, reveal five Raman peaks at 193, 478, 518, 617 and 687 cm^{-1} positions (Table 2), which correspond to the E_g, $3xF_{2g}$ and A_{1g} vibrational modes of the crystalline Co_3O_4, respectively [36]. Introduction of the Mg^{2+} ions led to a slight hipsochromic shift of the vibrations consistent with their smaller atomic mass (Fig. 3a and b). Upon substitution

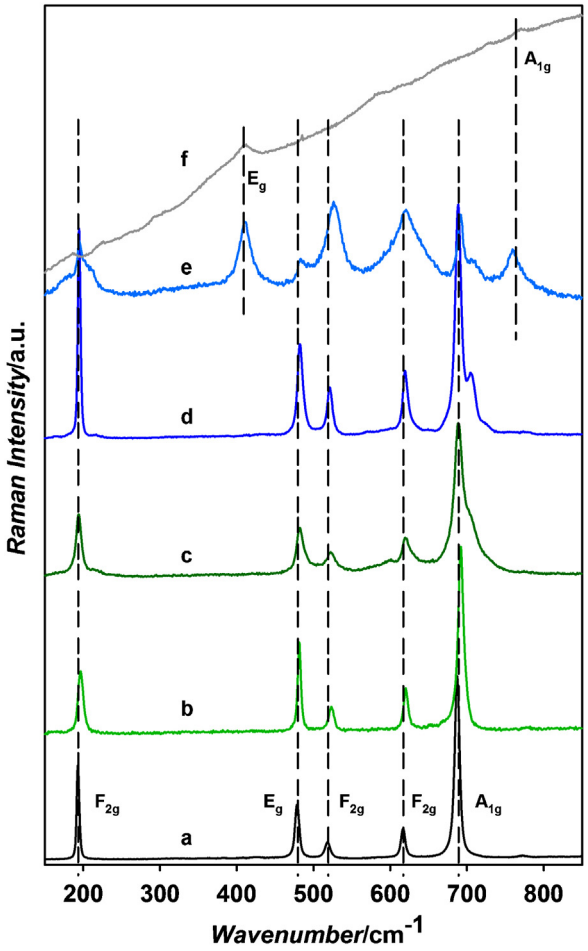

Fig. 3. Raman spectra of the investigated samples: (a) Co_3O_4; (b) $MgCo_2O_4$; (c) $MgCoAlO_4$; (d) $CoAl_2O_4$; (e) $Mg_{0.5}Co_{0.5}Al_2O_4$ and (f) $MgAl_2O_4$.

Table 2
Positions and assignments[a] of the Raman bands of the investigated spinel catalysts.

Band position/cm^{-1}	$F_{2g}^{(3)}$	E_g	$F_{2g}^{(2)}$	$F_{2g}^{(1)}$	A_{1g}
Co_3O_4	193.0	478.5	518.5	616.8	687.1
$MgCo_2O_4$	195.5	478.7	521.4	617.9	688.6
$MgAlCoO_4$	194.0	482.1	522.5	619.9	689.0
$CoAl_2O_4$	194.7	482.3	521.2	619.3	688.5
					704.7
$Mg_{0.5}Co_{0.5}Al_2O_4$*	195.0	410.6	526.7	620.6	691.8
		483.4			705.9
					760.0
$MgAl_2O_4$	–	409	–	–	768

[a] For the sake of brevity the modes are labelled as for parent Co_3O_4 spinel.

of the octahedral Co^{3+} ions by Al^{3+} ($MgCoAlO_4$) analogous feature at the high wavenumber side of the A_{1g} breathing oscillation bend [37] appeared, which is more distinguishable with the higher substitution level ($CoAl_2O_4$ and $Mg_{0.5}Co_{0.5}Al_2O_4$). This indicates that essentially, as intended, the Co^T was substituted by Mg^{2+} and Co^O, by the Al^{3+} ions, with a rather small inversion degree. For the latter sample, the features at 410.6 and 760.0 cm^{-1} are characteristic for a synthetic $MgAl_2O_4$ spinel, in agreement with the literature [38] and our experimental data (Fig. 3f). Generally, the intensity of the Raman signals was substantially decreased. This may indicate, apart from their more ionic character, cobalt distribution in the oxide matrix is naturally less ordered than for the pristine spinels, where each type of sites – octa- or tetrahedral are fully occupied by the same type of ions [39]. The doubling of the high-frequency A_{1g} band and the frequency shifts of Mg and Al containing spinels, compared with those of the corresponding mode in Co_3O_4, indicate some degree of inversion of the cobalt aluminate spinels, as reported previously [40].

3.3. XPS spectroscopy

The XPS survey scan showed that for all investigated spinels only the constituting elements were found on the catalysts surface. The diagnostic scan for Co2p energy range, shown in Fig. 4a–e, consists of several overlapping features originating from the $2p_{3/2}$ and $2p_{1/2}$ peaks due to Co^{2+} (780.6 and 795.9 eV) and Co^{3+} (779.4 and 794.5 eV) together with the associated satellite structure at 783.9–789.7 and 802.8 eV [41,42]. Upon introduction of Mg into Co_3O_4 the position and the shape of Co2p peaks do not change noticeably (Fig. 4a–c). However, the exchange of the octahedral Co^{3+} into Al^{3+} leads to the shift of the $Co2p_{3/2}$ peak energy of 0.6–0.8 eV towards higher binding energies (Fig. 4d, e). The satellite peak at 785.4 eV, well-manifested in the case of the $CoAl_2O_4$ and $Mg_{0.5}Co_{0.5}Al_2O_4$ catalyst and characteristic of Co^{2+} [41] cations confirms their intended presence in these samples. It can be thus inferred that for Co_3O_4 and $MgCo_2O_4$ cobalt is present in the form of the Co^{2+} and Co^{3+} cations, while for $CoAl_2O_4$ and $Mg_{0.5}Co_{0.5}Al_2O_4$

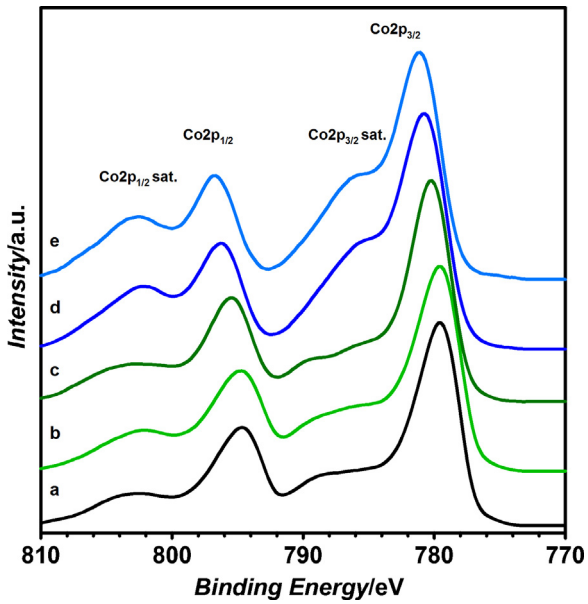

Fig. 4. XPS spectra in the Co2p range (A) and O1s (B) range: (a) Co_3O_4; (b) $MgCo_2O_4$; (c) $MgCoAlO_4$; (d) $CoAl_2O_4$; (e) $Mg_{0.5}Co_{0.5}Al_2O_4$ and (f) $MgAl_2O_4$.

the Co^{2+} cations dominate in the the near-to-surface region. The XPS surface composition of all the investigated catalysts is collected in Table 3. These data were further used in calculation of the turnover rates of N_2O decomposition as discussed below.

3.4. DFT calculations

The experimental investigations were supplemented by the DFT modelling. For Co_3O_4 the optimized lattice constant a and the u parameter are equal to 8.161 Å and 0.263, respectively, in good accordance with the corresponding experimental values

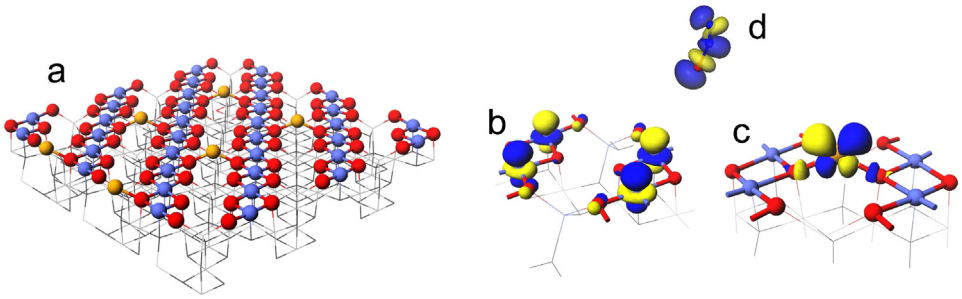

Fig. 5. The (1 0 0) spinel surface termination showing the dominant population of the octahedral sites (a). Orbital contours for Co^{Oh} (b) and Co^{Td} (c) centred orbitals together with the LUMO electron acceptor $3\pi^*$ of N_2O (d).

Table 3
XPS derived cationic chemical composition of the investigated spinel catalysts.

	Co	Mg	Al
Co_3O_4	100%	0%	0%
$MgCo_2O_4$	60 ± 6%	40 ± 6%	0%
$MgCoAlO_4$	26 ± 7%	18 ± 2%	56 ± 5%
$CoAl_2O_4$	16 ± 3%	0%	84 ± 3%
$Mg_{0.5}Co_{0.5}Al_2O_4$	12 ± 3%	8 ± 1%	80 ± 3%
$MgAl_2O_4$	0%	29 ± 1%	71 ± %

(Table 1). The calculated octahedral cobalt—oxygen and tetrahedral cobalt—oxygen bond lengths are equal to d_{Co^O-O} = 1.929 Å and d_{Co^T-O} = 1.933 Å, respectively. For the Mg-doped spinel the *a* and *u* values are equal to 8.151 Å and 0.264 and for Al_2CoO_4 to 8.170 Å and 0.26. Such small differences in the *u* and *a* values between pristine and doped cobalt spinels indicate that doping has very small influence on the overall oxide geometry, although it modifies the cationic sublattice appreciably.

The (1 0 0) spinel topmost ionic layer is presented in Fig. 5a. A strong difference of surface concentration between Co^O (blue) and Co^T (orange) active sites is apparent. In the case of the former the stripes of edge sharing octahedral are clearly visible. In Fig. 5b–d the HOMO donor orbital for Co^O (b) and Co^T(c) together with the LUMO electron acceptor $3\pi^*$ orbital (d) of N_2O molecule are presented. They are involved in the N_2O activation via electron transfer ($Co_{surf} \rightarrow$ LUMO $3\pi^* N_2O$). In the case of Co^T, since the donor orbital is dominated by d_{yz}, such overlap is less favourable due to a considerable symmetry mismatch. On the contrary, the Co^O donor orbitals are dominated by d_z^2 atomic orbitals. Protruding outside the catalyst surface they provide thereby a better spatial accessibility of the octahedral sites for sizeable 3d – $3\pi^* N_2O$ σ overlap of these redox orbitals. It naturally facilitates the first step of N_2O decomposition [15].

3.5. N_2O decomposition tests

The deN_2O reactivity results for all samples are shown in Fig. 6a–f along with the corresponding onsets of the H_2-TPR curves (Fig. 6a′–e′). The S-shaped conversion profiles reveal pronounced differences in the deN_2O reactivity pattern, well reproduced in an analogous sequence in the spinel catalysts reducibility. Such correlation has been already noted and discussed for similar oxide systems elsewhere [10]. However, it should be emphasised here, that due to pronounced differences in the crystallites shapes and diameters (10–260 nm) between the investigated spinel samples, in the case of complete bulk reduction the reversible redox processes of catalytic relevance are severely obscured by diffusion, segregation and new phase formation reactions [43]. Thus, the incipient reduction temperatures observed in the H_2-TPR profiles are more suitable to be directly correlated with the catalytic activity than the reduction maxima associated with much more pronounced bulk structural changes of the spinel catalyst. Using the procedure explained in the experimental section, the reaction rates (r/nmol$_{N_2O}$ × m^{-2} × s^{-1}) and turnover rates (TOR/s^{-1}) were calculated for all the investigated catalysts as a function of temperature. The comparison of the reaction rate and TOR curves shows that elimination of cationic redox centres by replacement of cobalt in tetrahedral and octahedral sites by magnesium and aluminium ions, respectively, results in a dramatic quenching of the catalytic activity (Fig. 7A and B). An appreciable conversion is observed only above 600 °C, indicating that the non-redox Mg^{2+} and Al^{3+} ions are essentially catalytically inert. Partial selective substitution by Mg^{2+} and Al^{3+} allowed for unravelling the catalytic role of the tetrahedral and octahedral cobalt ions in a direct way. Indeed, the replacement of the tetrahedral centres by magnesium gives rise to rather small

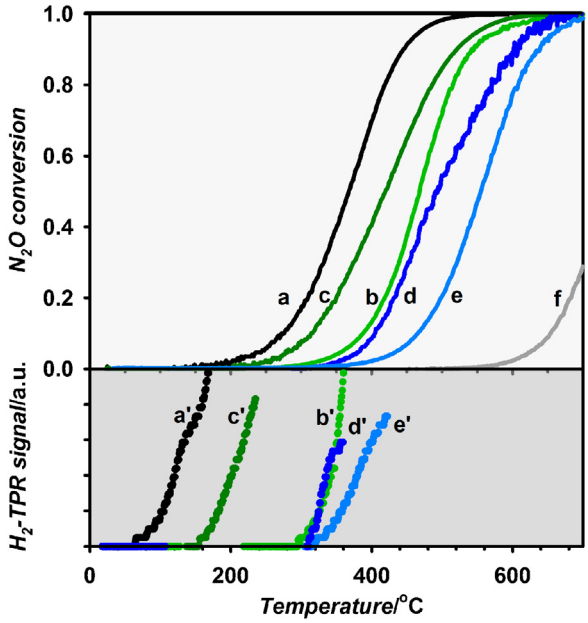

Fig. 6. N_2O conversion curves (a–f) and low temperature range reducibility patterns (a′–e′) for (a) Co_3O_4; (b) $MgCo_2O_4$; (c) $MgCoAlO_4$; (d) $CoAl_2O_4$; (e) $Mg_{0.5}Co_{0.5}Al_2O_4$ and (f) $MgAl_2O_4$.

decrease in the activity (the shift of the reaction window of about 50 °C to higher temperatures), substitution of the half of octahedral Co^{3+} centres increases the reaction temperature by 75 °C, whereas the complete elimination of the octahedral cobalt leads to much severe effect, moving the reaction window by more than 125 °C. These observations are also reflected in the dramatic changes in the corresponding activation energies: from 15 kcal mol^{-1} for Co_3O_4 and 17 kcal mol^{-1} for $MgCo_2O_4$, to 28 kcal mol^{-1} for $CoAl_2O_4$. Such

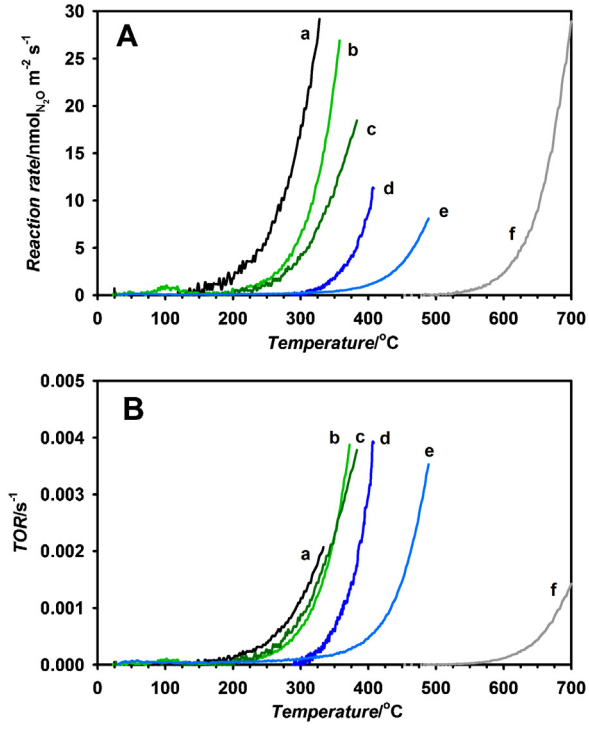

Fig. 7. Reaction rates (A) and the corresponding turnover rates (B) for N_2O decomposition as a function of temperature for (a) Co_3O_4; b) $MgCo_2O_4$; (c) $MgCoAlO_4$; (d) $CoAl_2O_4$; (e) $Mg_{0.5}Co_{0.5}Al_2O_4$ and (f) $MgAl_2O_4$.

results can be associated with the presence of octahedral Co^{3+} in the case of Co_3O_4 and $MgCo_2O_4$, and the tetrahedral Co^{2+} in $CoAl_2O_4$, showing the superior catalytic deN_2O activity of the octahedral centres in comparison to the tetrahedral ones. The activation barrier increases to 46 kcal mol^{-1} upon elimination of both cobalt redox sites giving rise to the observed poor catalytic activity of $MgAl_2O_4$ spinel (Fig. 7Af, Bf).

The accepted redox mechanism of N_2O decomposition comprises three most important elementary steps [1,4,15,20]: (i) cleavage of the N_2—O bond and formation of surface peroxy intermediate, initiated by electron transfer from active centres to nitrous oxide, (ii) surface diffusion of the peroxy species, and (iii) their final recombination into dioxygen. The latter closes the catalytic redox cycle by returning the electrons to active site. At first glance, the Co^{2+} cations might naturally appear as suitable candidates for the active sites for activation of N_2O molecule, as indeed it has been claimed elsewhere [10]. However, preservation of high activity of cobalt spinel when this cations were meticulously substituted by non-reducible Mg^{2+}, clearly contradicts assignment of tetrahedral Co^{2+} cations as the actual active sites for deN_2O reaction over Co_3O_4. On the contrary, analogous replacement of the octahedral Co^{3+} ions by Al^{3+} results in drastic decrease of the catalytic activity, revealing their actual role of primary active sites. As discussed above, the redox d_z^2 orbitals of the octahedral cobalt ions are easily accessible to reactants, facilitating the first step of N_2O decomposition. Moreover, it is the desorption of the dioxygen molecule that is reported to be the rate determining step of the deN_2O process [19,26]. In such a case, the Co^{3+} cations are responsible for oxidation of surface peroxy species ($O_2^{2-} \rightarrow O_2$) by accepting the released electrons. This conclusion is also indirectly supported by our recent investigations with the use of isotopically labelled $^{15}N_2{}^{18}O$ [44].

Comparison of the calculated turnover rates for all the investigated spinel catalysts is shown in Fig. 7B. In the case of Co_3O_4, $MgCo_2O_4$ and $MgCoAlO_4$ it can be concluded that the reactivity of these oxides is proportional to the number of the exposed cobalt ions. For the spinels with the cobalt ions located mainly in tetrahedral sites ($CoAl_2O_4$ and $Mg_{0.5}Co_{0.5}Al_2O_4$) their intrinsic reactivity, though being dramatically improved with respect to $MgAl_2O_4$, still remains distinct, indicating that the distortion of the spinel tetrahedra caused by the presence of the alien cations are reflected in the reactivity. In contrast, the merged TOR profiles for Co_3O_4, $MgCo_2O_4$ and $MgCoAlO_4$ samples (Fig. 7B) reveal that the intrinsic activity of the octahedral cobalt can be reliably assigned regardless the nature of the co-cation.

4. Conclusions

A series of cobalt spinels with redox Co^{2+} and Co^{3+} cations replaced by non-redox Mg^{2+} and Al^{3+} cations, respectively (Co_3O_4, $MgCo_2O_4$, $MgCoAlO_4$, $CoAl_2O_4$, $Mg_{0.5}Co_{0.5}Al_2O_4$ and $MgAl_2O_4$) was investigated in the catalytic decomposition of nitrous oxide. The key role of cobalt(III) cations serving as the primary active sites for N_2O decomposition was definitely revealed by means of XPS, UV–vis and Raman spectroscopy in conjunction with catalytic test studies. The determined activation energies, as well as turnover reaction rates indicate that the Co ions located in the octahedral sites exhibit high activity, whereas the cobalt ions located in the tetrahedral sites are distinctly less active. These experimental findings were corroborated with DFT calculations, which showed also better spatial accessibility of the HOMO (electron donor) orbitals of the octahedral cobalt for approaching reactant molecules, which facilitates the first step of nitrous oxide decomposition via surface–N_2O electron transfer mechanism. Since many cobalt oxide systems (such as spinels or hydrotalcite derived mixed oxides) are investigated as deN_2O catalysts, the results presented in this paper can be used as a starting approach for their rational optimisation through structural doping with alien cations.

Acknowledgements

The project was financed by the Polish National Science Centre awarded by decision number DEC-2011/03/B/ST5/01564.

The research was carried out with the equipment purchased thanks to the financial support of the European Regional Development Fund in the framework of the Polish Innovation Economy Operational Programme (contract no. POIG.02.01.00-12-023/08).

References

[1] J. Pérez-Ramírez, F. Kapteijn, K. Schöffel, J.A. Moulijn, Applied Catalysis B 44 (2003) 117–151.
[2] S. Parres-Esclapez, M.J. Illán-Gómez, C.S.-M. de Lecea, A. Bueno-López, Applied Catalysis B 96 (2010) 370–378.
[3] J.P. Dacquin, C. Dujardin, P. Granger, Journal of Catalysis 253 (2008) 37–49.
[4] W. Piskorz, F. Zasada, P. Stelmachowski, O. Diwald, A. Kotarba, Z. Sojka, Journal of Physical Chemistry C 115 (2011) 22451–22460.
[5] L. Obalová, G. Maniak, K. Karásková, F. Kovanda, A. Kotarba, Catalysis Communications 12 (2011) 1055–1058.
[6] P. Stelmachowski, F. Zasada, W. Piskorz, A. Kotarba, J.-F. Paul, Z. Sojka, Catalysis Today 137 (2008) 423–428.
[7] K. Karásková, L. Obalová, K. Jirátová, F. Komanda, Chemical Engineering Journal 160 (2010) 480–487.
[8] K. Jíša, J. Nováková, M. Schwarze, A. Vondrová, S. Sklenák, Z. Sobalik, Journal of Catalysis 262 (2009) 27–34.
[9] M. Haneda, Y. Kintaichi, H. Hamada, Applied Catalysis B 55 (2005) 169–175.
[10] K. Asano, C. Ohnishi, S. Iwamoto, Y. Shioya, M. Inoue, Applied Catalysis B 78 (2008) 242–249.
[11] F. Zasada, P. Stelmachowski, G. Maniak, J.-F. Paul, A. Kotarba, Z. Sojka, Catalysis Letters 127 (2009) 126–131.
[12] P. Stelmachowski, G. Maniak, A. Kotarba, Z. Sojka, Catalysis Communications 10 (2009) 1062–1065.
[13] N. Liu, R. Zhang, B. Chen, Y. Li, Y. Li, Journal of Catalysis 294 (2012) 99–112.
[14] S.-H. Wei, S.B. Zhang, Physical Review B 63 (2001) 045112.
[15] W. Piskorz, F. Zasada, P. Stelmachowski, A. Kotarba, Z. Sojka, Catalysis Today 137 (2008) 418–422.
[16] P. Pietrzyk, F. Zasada, W. Piskorz, A. Kotarba, Z. Sojka, Catalysis Today 119 (2007) 219–227.
[17] N. Pasha, N. Lingaiah, P. Siva Sankar Reddy, P.S. Sai Prasad, Catalysis Letters 127 (2009) 101–106.
[18] P. Stelmachowski, F. Zasada, G. Maniak, P. Granger, M. Inger, M. Wilk, A. Kotarba, Z. Sojka, Catalysis Letters 130 (2009) 637–641.
[19] L. Xue, Ch. Zhang, H. He, Y. Teraoka, Applied Catalysis B 75 (2007) 167–174.
[20] N. Russo, D. Fino, G. Saracco, V. Specchia, Catalysis Today 119 (2007) 228–232.
[21] M.A. Zamudio, S. Bensaid, D. Fino, N. Russo, Industrial and Engineering Chemistry Research 50 (2011) 2622–2627.
[22] R.A. Young, A. Sakthivel, T.S. Moss, C.O. Paiva-Santos, Journal of Applied Crystallography 28 (1995) 366–367, update of DBWS-9411.
[23] O. Levenspiel, Chemical Reaction Engineering, third ed., John Wiley & Sons, New York, 1999.
[24] L. Obalová, K. Jirátová, K. Karásková, F. Kovanda, Chinese Journal of Catalysis 32 (2011) 816–820.
[25] EUROKIN_fixed-bed_html, EUROKIN spreadsheet on requirements for measurement of intrinsic kinetics in the gas-solid fixed-bed reactor, 2012, www.eurokin.org
[26] F. Kapteijn, J. Rodriguez-Mirasol, J.A. Moulijn, Applied Catalysis B 9 (1996) 25–64.
[27] L. Obalová, V. Fíla, Applied Catalysis B 70 (2007) 353–359.
[28] F. Zasada, W. Piskorz, P. Stelmachowski, A. Kotarba, J.-F. Paul, T. Płocinski, K.J. Kurzydłowski, Z. Sojka, Journal of Physical Chemistry C 115 (2011) 6423–6432.
[29] J.J. Hafner, Computers and Chemistry 29 (2008) 2044–2078.
[30] V.I. Anisimov, J. Zaanen, O.K. Andersen, Physical Review B 44 (1991) 943–954.
[31] G. Kresse, J. Joubert, Physical Review B 59 (1999) 1758–1775.
[32] Ch.-S. Cheng, M. Serizawa, H. Sakata, T. Hirayama, Materials Chemistry and Physics 53 (1998) 225–230.
[33] K.J. Kim, Y.R. Park, Solid State Communications 127 (2003) 25–28.
[34] H. Keppler, N. Bagdassarov, Chemical Geology 158 (1999) 105–115.
[35] D. Rangappa, T. Naka, A. Kondo, M. Ishii, T. Kobayashi, T. Adschiri, Journal of the American Chemical Society 129 (2007) 11061–11066.

[36] V.G. Hadjiev, M.N. Iliev, I.V. Vergilov, Journal of Physics C 21 (1988) L199–L201.
[37] J. Preudhomme, P. Tarte, Spectrochimica Acta 27A (1971) 1817–1835.
[38] A.K. Kushwaha, Physica B 405 (2010) 2795–2798.
[39] G. Gouadec, P. Colomban, Progress in Crystal Growth and Characterization of Materials 53 (2007) 1–56.
[40] H. Furuhashi, M. Inagaki, S. Naka, Journal of Inorganic and Nuclear Chemistry 35 (1973) 3009–3014.
[41] S.C. Petitto, E.M. Marsh, G.A. Carson, M.A. Langell, Journal of Molecular Catalysis A 281 (2008) 49–58.
[42] F. Pepe, M. Occhiuzzi, Journal of the Chemical Society, Faraday Transactions 90 (1994) 905–910.
[43] D. Potoczna-Petru, L. Kepinski, Catalysis Letters 73 (2001) 41–46.
[44] G. Maniak, P. Stelmachowski, A. Kotarba, Z. Sojka, V. Rico-Pérez, A. Bueno-López, Applied Catalysis B 136–137 (2013) 302–307.